Direct force measurement of microscopic droplets pulled along soft surfaces

DIRECT FORCE MEASUREMENT OF MICROSCOPIC DROPLETS PULLED ALONG SOFT SURFACES

BY

HAMZA KHATTAK, B.Sc.

A THESIS

SUBMITTED TO THE DEPARTMENT OF PHYSICS & ASTRONOMY

AND THE SCHOOL OF GRADUATE STUDIES

OF MCMASTER UNIVERSITY

IN PARTIAL FULFILMENT OF THE REQUIREMENTS

FOR THE DEGREE OF

MASTER OF SCIENCE

Master of Science (2020)   McMaster University

(Physics & Astronomy)   Hamilton, Ontario, Canada

TITLE: Direct force measurement of microscopic droplets pulled

                           along soft surfaces

AUTHOR: Hamza Khattak

                           B.Sc.

SUPERVISOR: Dr. Kari Dalnoki-Veress

NUMBER OF PAGES: x, 56

Abstract

When a droplet is placed on a soft material, surface tension forces from the droplet are able to deform the substrate. This thesis explores the effect of substrate stiffness on energy dissipation as a droplet is slid along a soft material. We find behaviour is characterised by two regimes separated by the lengthscale of the deformation in the substrate. For films approximately the lengthscale of the deformation, dissipation increases with thickness. As the thickness becomes much larger than the size of deformation, there is a plateau in dissipation. This result agrees with the model we use to understand energy dissipation in these systems.

Acknowledgements

Whenever discussing graduate student life, the supervisor-student relationship is always central. I therefore consider myself very fortunate that I hit the supervisor jackpot. Thank you so much Kari for your support, guidance and for your focus on making sure we enjoy our time at Mac. I'm excited for the next 4 years of fun.

Thanks to KDVLab for being so awesome to work with. Messing around in the lab is so much more fun with the group. Many a scheme has been enhanced by your ideas and the graduate school experience would not be the same without you.

I would like to give a huge thanks my family and friends for being so wonderful. We are a product of our environment and I'm hugely fortunate that mines has been so supportive.

Finally, a shout out to the animals and tractor on the farm for making the lockdown a bit more fun.

Contents

List of Figures

viii

Chapter 1

Introduction

The motion of droplets is a phenomenon ubiquitous to everyday life from oil slid-
ing around a pan to cactus needles channelling water into their stems. In each of
these cases there is an interplay between several physical effects driving the overall
behaviour. For example, to understand a water droplet moving across a glass car
window, we must consider a balance between the effects of surface tension, internal
fluid interactions and external forces including gravity and air resistance. The prob-
lem comes down to some set of inputs that modify the droplet behaviour. However,
what about the effect the droplet has on its environment? In a stiff substrate such
as glass, we can ignore what the droplet does to the glass, since the droplet cannot
measurably deform the substrate. However, what if the substrate is soft enough to
be deformed by surface tension?

Recently, such soft materials have been developed, resulting in a growing field of
research into studying droplet-soft material interactions [2–5]. Studies in the field
have varied from using geometric softness control to create droplet motion [6] to the
anisotropic deformation of droplets as a result of stretched films [7]. With a physical

understanding of such systems also come possible applications ranging from microflu-
idics [8] to water collection [9]. One fundamental question in this field is how energy
is dissipated as droplets move across these substrates. There has been research into
dissipation with larger droplets [10–12], however, dissipation in microscopic droplets
on soft substrates remains unexplored. At smaller length-scales the importance of
surface tension becomes larger and the relevance to applications such as microflu-
idics increases. We are therefore interested in understanding droplet-soft substrate
dissipation in the microscopic regime.

In chapter 1 we introduce the physical concepts necessary to understand the ex-
periments and model employed in this thesis. In section 1.1 we discuss the general
aspects and molecular origin of surface tension. In 1.2 we explore wetting, or how
surface tension results in the formation of droplet. In 1.3 we explore continuum me-
chanics and how it can be used to address wetting on soft substrates. Finally in 1.4
we introduce motion and dynamic wetting in soft substrates.

With a theoretical background established in chapter 1, chapter 2 outlines how
the samples were prepared, experiments conducted and data analysed. To control
the effective softness of our substrates, we modify substrate thickness. To measure
dissipation of droplets moving across these substrates we use a micropipette based
force measuring technique. Finally, chapter 3 includes experimental results and a
scaling model for soft substrate dissipation with varying thickness films. We find that
above a cutoff thickness, thicker films dissipate more energy.

1.1   Surface tension and surface energies

1.1.1   Basic Principles

To develop the physics relevant to wetting on soft materials, we first establish relevant definitions. These definitions can be developed from a simple cartoon model of a liquid-vapour interface (Fig. 1.1a). We see that molecules at the surface of the liquid have fewer attractive interactions than those in the bulk. These interactions reduce the free energy of the molecule and therefore there is a free energy cost per unit area of an interface which is referred to as the interfacial energy. [1, 13]:

$$\gamma = \left(\frac{\partial F}{\partial A} \right)_{T,V,N} .$$

(1.1)

We can connect this interfacial energy to a force by using an additional cartoon (Fig. 1.1b) and the virtual work principle [1]. First we superimpose an imaginary square of sidelength L on an interface with some energy cost per unit area γ. If we now translate a side of this square by a distance dl The energy of the interface increases by $L\gamma dl$. This implies a force per unit width parallel to the translation direction which is defined in the surface tension tensor, $\overline{\overline{\Upsilon}}$. In liquids this surface tension is isotropic and can simply be given by by the surface energy $\gamma\delta_{ij}$. However, the tension-energy equivalence does not necessarily hold in certain soft materials so it is useful in some cases to keep the definitions separate.
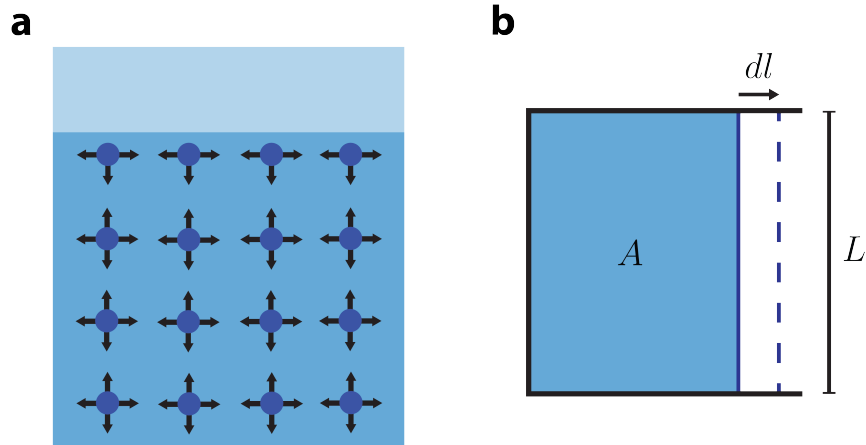
Figure 1.1: a) Commonly used cartoon model for the molecular origin of surface tension. b) Virtual work principle diagram to relate the change in surface energy to a surface tension force.

1.1.2   Molecular description

Although the basic description in Fig 1.1a is useful for making definitions and as a thermodynamic explanation for surface tension, it is also useful to have a molecular description. Indeed, looking at the surface molecules in Fig. 1.1a, there appears to be a net force perpendicular to the surface which is contrary to an expected surface tension parallel to the surface.

To address the apparent inconsistency between bulk and molecular behaviour we look at the limitations of the simple model in Fig. 1.1a. The first of these limitations is an assumption of purely attractive interactions between molecules in the liquid phase. While these attractive interactions may be stronger averaged over all molecules, the force is distance dependant. This behaviour is commonly modelled with a Lennard-Jones potential [1] (Fig. 1.2). The shorter range forces in these systems are isotropic
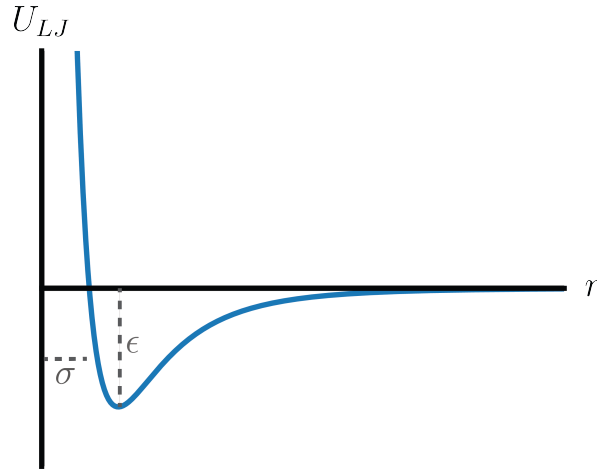
Figure 1.2: Example of a Lennard-Jones plot or intermolecular potential vs radius that empirically fits the combination of attractive and repulsive interactions between molecules. The form of this curve is given by $U_{LJ} = 4\epsilon \left[\left(\frac{\sigma}{r} \right)^{12} - \left(\frac{\sigma}{r} \right)^{6} \right]$ where σ is a lengthscale representing the intermolecular interaction distance and ε gives the depth of the potential well as shown in the plot.

and we can treat them as hard shells that are mostly independent of the molecular environment [1]. The attractive interactions, on the other hand, are much longer ranged and can be influenced by the environment including by changed environments found at surfaces [1]. Along with the simplifications in bonding, the model model in Fig. 1.1a also assumes a binary step-like interface. In reality, allowing for thermal fluctuations, there will be a finite sized transition in density between the two phases [14].

We can incorporate these new concepts to a new model illustrated in Fig. 1.3 (adapted from [1]). In this model we draw out small volumes in equilibrium at different distances from the interface. We split the forces acting on these volumes into attractive and repulsive components. We also split the forces into components parallel

and normal to the surface (Fig. 1.3a). We note that the repulsive forces are isotropic and will only depend on the density which increases with depth. The equilibrium condition, combined with a lack of symmetry (i.e. lower forces above) means that in the normal direction repulsive forces must be balanced by attractive forces. However, looking at the parallel plane, density is constant meaning attractive and repulsive forces may be imbalanced. While the repulsive isotropic forces show the same depth behaviour they did in the vertical direction, the long range attractive forces show weaker depth dependence and there is an enhanced attractive force between molecules which is referred to as surface tension (Fig. 1.3b) [1].

Molecular dynamics simulations have been completed on such interfaces which shown the validity of this picture [15–17]. For the typical intermolecular bond strengths of liquids $E \sim kT$ (here k is the Boltzmann constant and T is the temperature), simulations show the lengthscale of the molecular concentration gradient is on the order of the average intermolecular distance [1]. The molecular concentration gradient results in a density transition occurring over fractions of a nm, L_{DT}. Above this lengthscale, we can treat surface tension effects as a boundary condition in a continuum problem. With a continuum treatment, we are able to more simply determine some of the consequences of such a horizontal force at an interface.

1.1.3   Laplace Pressure

The Laplace pressure refers to the pressure differential across a curved interface as a result of the interfacial energy cost. To illustrate why surface energy leads to Laplace pressure, we use the simplest case of a small volume of liquid surrounded by a gas in

---

[1]There is some additional physics that arises when considering a solid-liquid interface where the liquid also interacts with the solid (see [1]), however, we can still use a surface tension formulation.
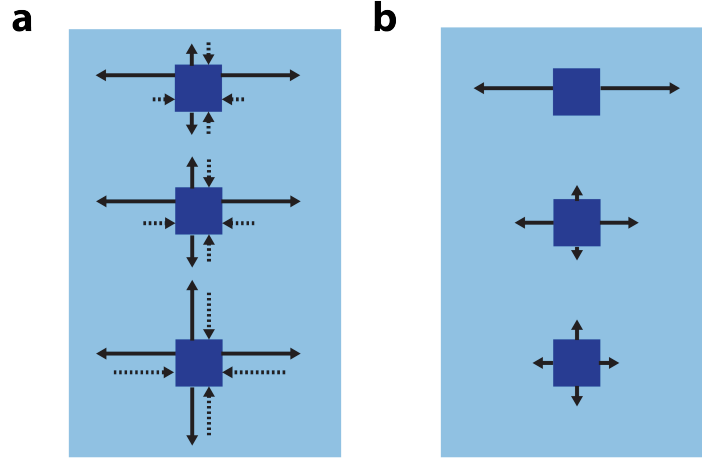
Figure 1.3: Molecular model of surface tension adapted from [1]. Solid arrows indicate attractive forces and dotted arrows indicate repulsive forces. a) Forces along the vertical and horizontal directions split into attractive and repulsive forces. c) Net force after summing the results of plot a.

the absence of external forces. In this case we can write the work done by the liquid drop as follows[13]:

$$\delta W = -p_l dV_l - p_v dV_v + \gamma dA \,. \tag{1.2}$$

Where we have terms accounting for the pressure work, pdV, and the work to overcome surface tension, γdA. We account for the separate work on each volume with subscripts l and v for liquid and vapour respectively. The volume with the lowest surface area is a sphere so we expect $dV_l = -dV_v = 4\pi R^2 dR$ and $dA = 8\pi R dR$ where R is the radius of a circle. Using these relations and applying an equilibrium condition, $\delta W = 0$, we get:

$$\delta p = p_l - p_v = \frac{2\gamma}{R} \,. \tag{1.3}$$

This equation can be generalised to a surface with arbitrary curvature to give what is known as the Laplace pressure. [13]:

$$\delta p = \gamma \left(\frac{1}{R} + \frac{1}{R'} \right) = \gamma C \,, \tag{1.4}$$

where R and R' are radii of curvature and C is the curvature. The consequence of this relation is that liquids will tend to maintain constant curvature. Out of equilibrium, a liquid will flow to a region of lower curvature. This phenomenon is what drives, for example, water flow towards the base of cactus needles [18]. In the case of interest here, if we want to create flow in droplets, we must induce lower curvature in the direction of motion.

1.1.4   Energy scale and capillary length

To get a sense for the actual magnitude of these interfacial energies for a typical liquid, we can use a simple thermodynamic scaling argument. We expect in a given unit area at the surface that the number of bonds is proportional to $\frac{1}{\sigma^2}$ where σ is an average intermolecular distance. We also know the energy, ϵ, of each of these bonds and multiply to get:

$$\gamma \sim \frac{\epsilon}{\sigma^2} \,. \tag{1.5}$$

For most liquids where van der Waals forces are the dominant intermolecular interaction ($\epsilon\ kT$) this formulation gives γ of order $10\,\mathrm{mJ/m^2}$ which matches experimental measurements [1].

Along with having an absolute value, comparison to gravitational energies in a system can be helpful to determine whether we need to include gravity in our analysis.

We can equate the Laplace pressure (γ/R) and the hydrostatic pressure due to gravity $\sim \rho g R$ to get the gravity capillary length L_{GC} [13]

$$L_{GC} = \sqrt{\frac{\gamma}{\rho g}} \, . \tag{1.6}$$

Below this lengthscale, which is of order mm for many liquids, we can safely ignore the effect of gravity on the system. Here we study systems with sizes $<< L_{GC}$ and therefore, unless otherwise noted, we will work under the assumption that gravity can be ignored.

1.2 Wetting

1.2.1 Definitions

Wetting is generally defined as the spreading of a liquid deposited on a substrate (which can be liquid or solid). Depending on the strength of system interfacial interactions, wetting can be split into two regimes which depend on a wetting parameter S. For a liquid droplet on a solid surface we define:

$$S = \gamma_{sv} - (\gamma_{sl} + \gamma_{lv}) \, ; \tag{1.7}$$

where each γ is the interfacial energy, with the two materials in contact defined by by the subscript (s for solid, l for a liquid and v for a vapour). If $S > 0$ the lowest energy configuration is simply a maximally spread liquid layer (Fig. 1.4a). However, if $S < 0$ there is a competition between minimising the region wetted by the droplet and minimising the area of the liquid-gas interface. This results in a contact angle, θ

a   **b**

$$S > 0 \qquad\qquad\qquad S < 0$$
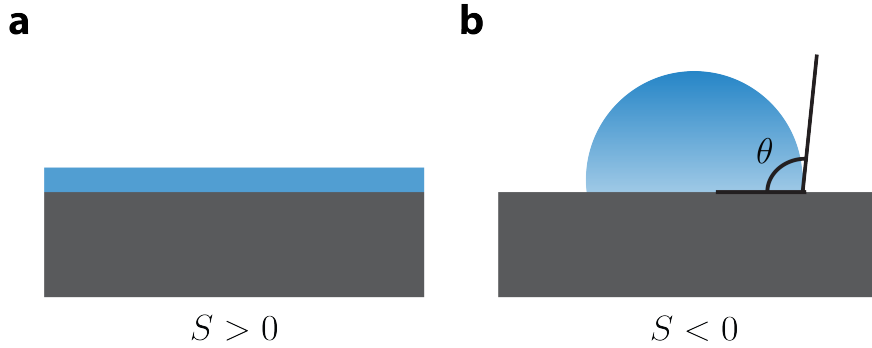
Figure 1.4: a) Maximally spread layer from $S > 0$. b) Partial wetting ($S < 0$) where there is a defined contact angle.

between the substrate and the droplet 1.4b). We will be considering only cases where $S < 0$ and there is a non-zero contact angle for the interface.

1.2.2 Simple cases of wetting

It is possible to treat some simple cases of wetting with arguments based on a force balance at the contact line and Laplace pressure. In these models interfacial energy is assumed to be equivalent to interfacial tension and so γ and Υ are used interchangeably. Young's equation is a classical equation in wetting that relates the contact angle of a droplet on a stiff surface to interfacial tensions. The standard formulation for Young's equation is described in Fig. 1.5a where a horizontal force balance is performed on the edge of a droplet. Simple vector summation along the horizontal leads to Young's equation:

$$\gamma_{sv} = \gamma_{sl} + \gamma_{lv}\cos\theta\,. \tag{1.8}$$

This equation defines the contact angle of the droplet, θ, as a function of its interfacial energies. At equilibrium, the droplet must also have a constant internal pressure.
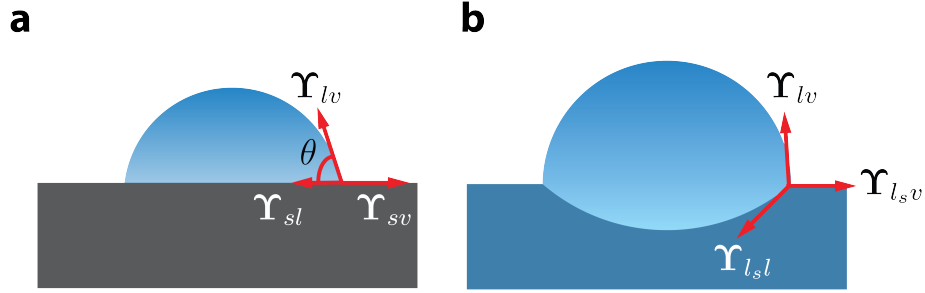
Figure 1.5: fig:a) Illustration of force balance at contact line at stiff balance to derive Young's equation. b) Droplet on liquid substrate illustrating the Neumann force balance at the contact line and formation of two curved surfaces.

Using the Laplace equation (eq 1.4) we then know the droplet will be a constant curvature spherical cap. Although the Young's equation is useful in many instances, we note that the force at the contact line is not balanced in the vertical direction (Fig. 1.5a). This is since the model assumes a sufficiently stiff substrate such that the forces exerted by the droplet on the the substrate can be ignored. We will see this is not the case with soft substrates.

On the other extreme of a stiff substrate is a liquid substrate. In such a case we can use the so called Neumann construction to get a prediction for droplet geometry. We note that at the edge of the droplet (Fig 1.5b) the total stresses must sum to 0, giving the Neumann condition which is expressed in a one plane vector as:

$$\Upsilon_{\mathbf{lv}} + \Upsilon_{\mathbf{l_s l}} + \Upsilon_{\mathbf{l_s v}} = 0 \,, \tag{1.9}$$

where we now also have a l_s subscript element to differentiate between the liquid

droplet, l, and liquid substrate, l_s [2]. Along with the Neumann condition constraint at the edge of the droplet, the shape of the droplet is also constrained by Laplace pressure requirements. Since the interface between the vapour and substrate liquid is uncurved at the relvant lengthscales, they must have equal pressure $p_v = p_{l_s}$. Also, the pressure inside the droplet must be constant to maintain equilibrium. We therefore have:

$$\gamma_{l_s l} C_{l_s l} = \gamma_{lv} C_{lv} \, . \tag{1.10}$$

With this set of equations, knowing surface tension, we can uniquely define the geometry of a droplet on a liquid substrate.

1.2.3 Energy minimisation

To demonstrate the validity of these force based methods we can use a more rigorous variational energy minimisation approach to solving wetting problems. In particular, we closely follow [19] to develop these techniques using a droplet on a stiff substrate. For simplicity, we will consider a one dimensional problem which reduces the droplet to a profile $h(x)$. If the droplet extends from a point a to a point b, we have the following contributions to the energy, noting the energy is proportional to path length.

$$\mathrm{Solid - Vapour} \qquad E = \int_{-\infty}^{a} \gamma_{sv} \, \mathrm{d}x + \int_{b}^{\infty} \gamma_{sv} \, \mathrm{d}x \, , \tag{1.11}$$

$$\mathrm{Solid - Liquid} \qquad E = \int_{a}^{b} \gamma_{sl} \, \mathrm{d}x \, , \tag{1.12}$$

$$\mathrm{Liquid - Vapour} \qquad E = \int_{a}^{b} \gamma_{lv} \sqrt{1 + h'^2} \, \mathrm{d}x \, . \tag{1.13}$$

---

[2]Note that when expressed as a vector, subscripts of $\boldsymbol{\Upsilon}$ represent materials. If not in vector form, i.e. $\boldsymbol{\Upsilon}_{ij}$, the subscripts represent elements of the surface tension tensor.

For the variational analysis, it is helpful to restrict all variables to a single integral so we define a function that gives the energy change in energy caused by the wetted region.

$$\Gamma(h, h') = \gamma_{lv}\sqrt{1 + h'^2} + \gamma_{sl} - \gamma sv \,. \tag{1.14}$$

This allows us to write out the energy in a more tractable form as :

$$E[h] = \int_a^b \Gamma(h, h') \, \mathrm{d}x + \int_{-\infty}^{\infty} \gamma_{sv} \, \mathrm{d}x \,,$$

$$E[h] = \int_a^b \Gamma(h, h') \, \mathrm{d}x + \text{const} \,. \tag{1.15}$$

We then note that the droplet volume is constant, $\int h \, \mathrm{d}x = V$, so add a Lagrange multiplier to our variation problem giving $\varepsilon = E - \lambda \int h \, \mathrm{d}x$. Performing this variation with variable limits a and b gives:

$$\delta E = \Gamma(b)\delta b - \Gamma(a)\delta a + \frac{\partial \Gamma}{\partial h'}\delta h|_a^b + \int_a^b \mathrm{d}x \left(\frac{\partial \Gamma}{\partial h} - \frac{\mathrm{d}}{\mathrm{d}x}\frac{\partial \Gamma}{\partial h'} - \lambda \right) \delta h \,. \tag{1.16}$$

At equilibrium we expect $\delta\varepsilon = 0$ for any given δh, thus in the bulk we expect the integral to vanish giving the Euler-Lagrange equation:

$$\frac{\partial \Gamma}{\partial h} - \frac{\mathrm{d}}{\mathrm{d}x}\frac{\partial \Gamma}{\partial h'} - \lambda = 0 \,. \tag{1.17}$$

Substituting in Γ gives $\lambda = \lambda_{lv}C$ where C is the curvature $(h''/(1 + h'^2)^{3/2})$ which matches the Laplace pressure equations from earlier (note that here primers are spatial derivatives). We can simplify further by multiplying 1.17 by h' and integrating to

yield a quantity $\mathscr{G}$ conserved along the surface:

$$\mathscr{G} = \gamma - h'\frac{\partial\Gamma}{\partial h'} + \gamma_{lv}Ch\,. \tag{1.18}$$

To solve eq. 1.18 we use the boundary conditions. We first perform a linear approximation for δa and δb in terms of δh (i.e. $\delta b = \delta h(a)/h'(a)$). The non integral part of eq. 1.16 must also be 0 for arbitrary δh giving:

$$-\frac{\Gamma}{h} + \frac{\partial\Gamma}{\partial h'} = 0\,. \tag{1.19}$$

Comparing this result to equation 1.19 at the boundaries when $h = 0$ we have:

$$\frac{\gamma_{lv}}{\sqrt{1 + h'^2}} - (\gamma_{sv} - \gamma sl) + \gamma_{lv}Ch = 0\,. \tag{1.20}$$

We note that we can express the slope as $\tan\theta$ and $h = 0$ at the contact line which means eq. 1.20 simplifies to Young's equation (eq. 1.7) at the contact line. This variational technique can be extended to work on a broad range of problems including soft substrates by adding additional energy terms [20].

1.3 Soft Substrates

1.3.1 Definitions

We first define some standard terminology in continuum mechanics. Stress is a force per unit area applied on a material. To fully define stresses on a material we consider an infinitesimal cube of material. If we apply a force normal to a plane of the cube,
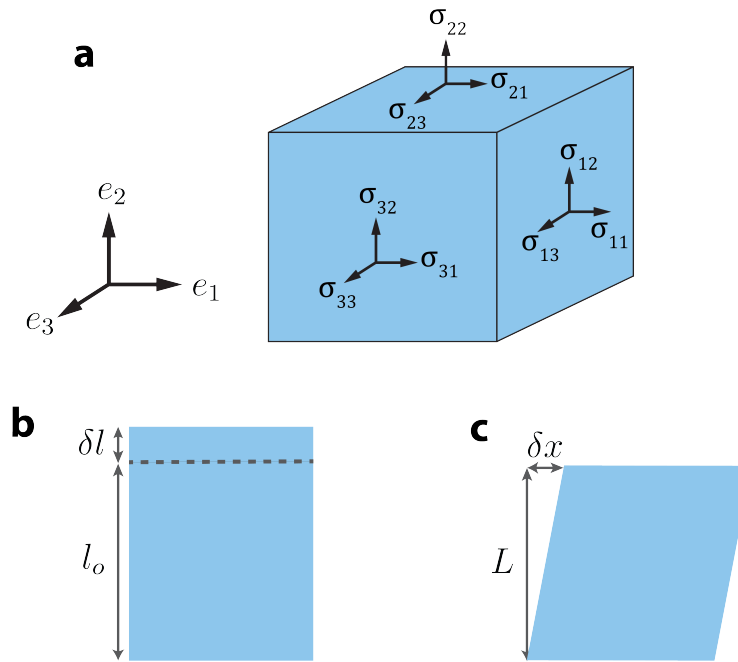
Figure 1.6: a) Definition of the standard Cauchy stress tensor using an infinitesimal box. b) Sketch to illustrate definition of traction strain. c) Sketch to illustrate definition of shear strain.

we have traction stresses (ie tension or compression). If we a apply a force parallel to one of the planes, we have a shear stress. The standard Cauchy stress tensor $\bar{\bar{\sigma}}$ compactly specifies all modes of stress acting on our infinitesimal box (Fig 1.6a).

These applied forces cause a deformation of the material which is referred to as the strain, ε. Strain can be any function that relates the deformation in a material to a reference length. Like stress, for a general description of strain on a material, we need to use a tensor formulation. We first define $\mathbf{X}$ as our undeformed configuration and $\mathbf{x}$ as the final configuration with a displacement vector $\mathbf{u} = \mathbf{x} - \mathbf{X}$. We first look at the transformation of the differential $d\mathbf{X}$. In this case, using $\mathbf{x} = \mathbf{x}(\mathbf{X})$ we can

write:

$$\mathrm{d}\mathbf{x} = \frac{\partial \mathbf{x}}{\partial \mathbf{X}} \, \mathrm{d}\mathbf{X} \ . \tag{1.21}$$

This allows us to define the so called deformation gradient, $\bar{\bar{\mathbf{F}}}$ [21]:

$$\bar{\bar{\mathbf{F}}} = \frac{\partial \mathbf{x}}{\partial \mathbf{X}} \tag{1.22}$$

$$= \boldsymbol{\nabla}_{\mathbf{X}}(\mathbf{x}) \tag{1.23}$$

$$F_{ij} = \frac{\partial x_i}{\partial x_j} \ . \tag{1.24}$$

This expression can also be rewritten in terms of $\mathbf{u}$ as $\bar{\bar{\mathbf{F}}} = \bar{\bar{\mathbf{I}}} + \frac{\partial \mathbf{u}}{\partial \mathbf{X}}$. We want our definition for strain to be specific to deformations and since $\bar{\bar{\mathbf{F}}} \neq \bar{\bar{\mathbf{I}}}$ when there is a rigid body rotation we introduce a new quantity called the Green-Lagrange strain tensor $\bar{\bar{\mathbf{E}}}$:

$$\bar{\bar{\mathbf{E}}} = \frac{1}{2} \left((\boldsymbol{\nabla}_{\mathbf{X}}\mathbf{u}) + (\boldsymbol{\nabla}_{\mathbf{X}}\mathbf{u})^T + (\boldsymbol{\nabla}_{\mathbf{X}}\mathbf{u})(\boldsymbol{\nabla}_{\mathbf{X}}\mathbf{u})^T \right) \ . \tag{1.25}$$

Finally, for small strains which will be the case for most of our analysis, we can ignore the final term and write the strain ε_{ij}:

$$\varepsilon_{ij} = \frac{1}{2} \left(\frac{\partial u_i}{\partial X_j} + \frac{\partial u_j}{\partial X_i} \right) \ . \tag{1.26}$$

Along with the more general strain tensor, we use some simpler formulations to define some commonly used quantities in mechanics. We first have a strain measure for traction forces, e (Fig 1.6b):

$$e = \left(\frac{\delta l}{l_o} \right) \ , \tag{1.27}$$

16

where δl is the change in object length after deformation and l_o the initial object length. For shear forces, we can define strain as (Fig 1.6c):

$$\lambda = \left(\frac{\delta x}{L} \right) , \tag{1.28}$$

where δx is the change along the direction of the applied stress and L is perpendicular to the stress plane.

If we have a simple elastic, Hookean material, we can use our strain definitions to also define some commonly used elastic moduli. We have the Young's modulus which applies to traction forces:

$$E \equiv \frac{\sigma}{\epsilon} . \tag{1.29}$$

The modulus for shear forces is simply known as the shear modulus, and given by:

$$G \equiv \frac{\sigma}{\lambda}. \tag{1.30}$$

We can also define the so called Poisson's ratio which is defined by the strain in a material perpendicular to the applied stress:

$$\nu = -\frac{\mathrm{d}e_{\perp\sigma}}{\mathrm{d}e_{\parallel\sigma}} . \tag{1.31}$$

A perfectly isotropic and incompressible elastically deformed material will have a Poisson's ratio of 0.5. In this case the material will have a constant density, with a change in length in one direction compensated by opposite changes in each of the perpendicular directions.

We can use these parameters for our definition of a "soft" substrate. We classify
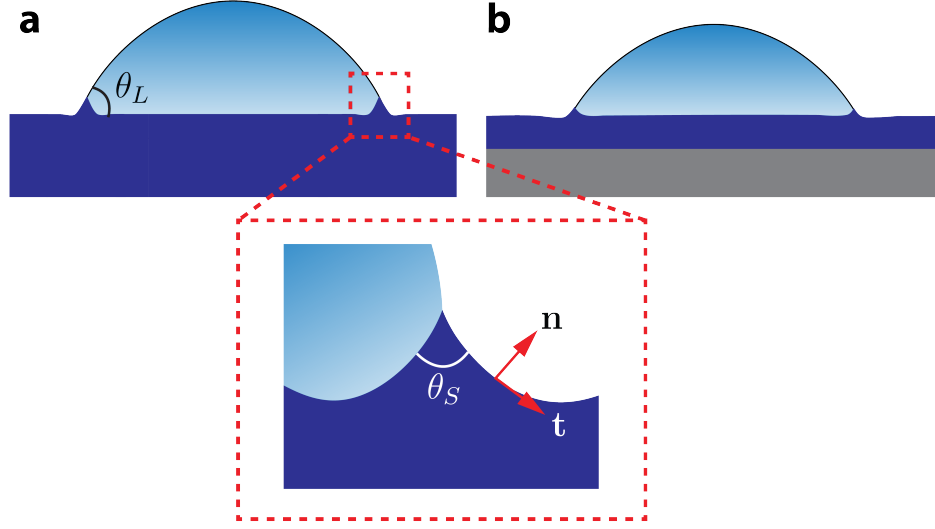
Figure 1.7: a) Droplet of a soft substrate with $R >> L_{EC} > L_{DT}$. Inset is zoom of the capillary ridge. b) Case where the soft layer has $h \sim L_{EC}$.

any solid material that can be deformed beyond the atomic scale by the stresses of surface tension as soft. To quantify softness in our context we use the elastocapillary length:

$$L_{EC} = \frac{\gamma}{G}, \tag{1.32}$$

where γ is interfacial energy as defined previously and G is the shear modulus. If L_{EC} is much greater than the transition lengthscale, L_{DT}, the forces of surface tension will deform the substrate (Fig. 1.7a). Although there are several regimes for soft wetting depending on droplet and substrate geometry we will assume our droplets radius, R, is much larger the the ridge size (Fig 1.7). We will also only consider either bulk soft substrates, or thin soft layers $h \sim L_{EC}$ on stiff substrates (Fig. 1.7b). This assumption helps split contact angle measurements into two distinct lengthscales. We define θ_S for the capillary ridge of the substrate (Fig. 1.7a) and θ_L for the droplet.

1.3.2   Cross-linked polymer networks

To determine if these continuum definitions of material properties are appropriate, we need a basic understanding of the physics of the particular soft substrate under study. In Fig. 1.8 we see a schematic arrangement of a polydimethylsiloxane (PDMS) network and the related lengthscales. At the most basic level, we have a monomer, whose size is governed by its chemical makeup. Generally, the lengthscale of these monomers are $a \sim 1\,\text{nm}$. Monomers are much smaller than the size of any geometric features we will consider and we therefore do not need an individual monomer picture.

If we create a chain with $N_a \gg 1$ monomers we have a polymer chain. To determine the lengthscale associated with these chains we use the freely jointed chain, or random walk, model. Rather than N_a monomers, We treat the polymer chain as made up of N_b randomly oriented, non-interacting, segments of length, b. Although this is a simple model, it is useful in many polymer systems and will be sufficient to find a chain lengthscale [22]. To define a lengthscale for the polymer we will use the radius of gyration:

$$R_g{}^2 = \frac{1}{N} \sum_i^N \left(\mathbf{r}_i - \mathbf{r}_{\text{CM}}\right)^2 \;, \tag{1.33}$$

where $\mathbf{r}$ specifies the segment locations and $\mathbf{r}_{CM}$ the center of mass. It can be shown that the average chain length, $\langle R_g \rangle \propto \sqrt{N}b$ [23]. Although R_g can vary greatly depending on the specific system of interest, typically $R_g \sim 10 - 100\,\text{nm}$. At these lengthscales, it is possible for geometric confinement effects to modify polymer properties [24, 25]. Since films of this lengthscale are possible to produce, this effect may need to be considered. Still, we can use a continuum picture with the use of an effective modulus of the thin film [25].

Finally, we look at the crosslinks between the chains. In the case of PDMS,
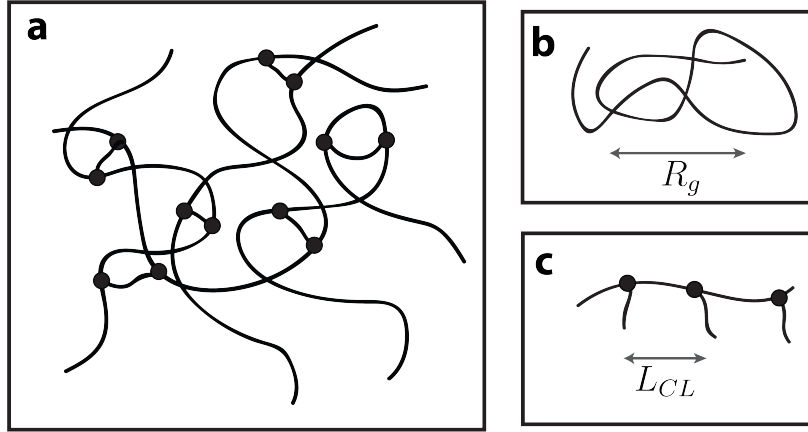
Figure 1.8: a) Sketch of a typical cross-linked rubber network. Black circles indicate covalent bonds whereas any other crossing lines are simply in another plane or physically entangled. b) Individual chain lengthscale illustration c) Crosslinking lengthscale illustration. Note that L_{CL} is point to point distance rather than a distance along the chain.

cross-linking involves chemical bonds between modified monomer sites of otherwise chemically similar chains (Fig.1.8a) . Since there are generally multiple cross-link sites per chain, the lengthscale between cross-link sites will smaller than R_g (Fig.1.8c), and we can generally ignore cross-linker confinement effects. [3]

1.3.3   Shuttleworth effect

When a soft substrate is strained, its interfacial energy may change. The consequence of this phenomenon is the loss of equivalence between interfacial energy and surface tension. We consider straining a box of length l_o by ϵ. If we use a surface tension formulation we use $\mathrm{d}W = F \cdot \mathrm{d}x$ noting $x = l\epsilon$. We then have the work per unit

---

[3]An alternative cross-linking mechanism involves chains with large alternating blocks of chemical structure. In this case the inhomogeneity can have a lengthscale comparable to R_g and effects of confinement on crosslinking would need to be considered.

length:

$$\frac{\delta W}{l_o} = \Upsilon l_o \, \delta\epsilon \ . \tag{1.34}$$

Looking at the same change from a interfacial energy perspective, for a small displacement we can write:

$$\frac{\delta W}{l_o} = \delta l \gamma \tag{1.35}$$

$$= \delta[l_o(1 + \epsilon)\gamma] \ . \tag{1.36}$$

Comparing 1.34 and 1.36 we arrive at the Shuttleworth equation [26]:

$$\Upsilon(\epsilon) = \frac{\mathrm{d}}{\mathrm{d}\epsilon}\left[(1 + \epsilon)\gamma(\epsilon)\right] = \gamma + (1 + \epsilon)\frac{\mathrm{d}\gamma}{\mathrm{d}\epsilon} \ . \tag{1.37}$$

This correction becomes necessary in the case of either pre-stretched substrates, or those with especially large deformations where $\nu \neq \frac{1}{2}$.

1.3.4   Boundary Conditions

In the case of soft substrates there are two modes of surface deformation and each mode has its own boundary conditions. Following [20] we consider a capillary ridge much larger than any atomic effects (Fig. 1.7). We define $\mathbf{t}$ and $\mathbf{n}$ as vectors parallel and normal to the interface. We also define a curvilinear coordinate s that runs along the solid interface, contacting the droplet at a point $s = r$. If we perform a stress

balance at any point along the substrate in contact with the liquid:

$$\bar{\bar{\sigma}} \cdot \mathbf{n} - \bar{\bar{\mathbf{T}}} \cdot \mathbf{n} = \frac{\partial}{\partial s}(\Upsilon \mathbf{t}) \,, \tag{1.38}$$

$$\sigma_s - \sigma_l = \frac{\partial}{\partial s}(\Upsilon \mathbf{t}), \tag{1.39}$$

where σ_s is the elastic traction and σ_l is the liquid traction (ie tension compression parts of stress tensors). Looking at an infinitesimal region around the contact line $(s = r)$ this simplifies to the same Neumann's law that is used for liquids [27]. This condition provides a constraint on translations of the contact line. Written in terms of our new vectors $\mathbf{t}$ and summing over our interfaces i we have our first boundary condition:

$$\sum_i \upsilon_i \mathbf{t}_i = 0 \,. \tag{1.40}$$

For our second boundary condition, we imagine the scenario in (Fig. 1.7). In this case there is no translation of the contact ridge, however, there is a change in free energy from different portions of the substrate being wetted. This implies a lack of resistance to sliding in the substrate and is therefore referred to as the "no pinning" boundary condition. By considering the energy cost of this sliding variation (ie changing the value of r in Fig. 1.7), it is also possible to derive a boundary condition for this case (see [20]) as a function of strain, ϵ, and the gradient of elastic energy $\frac{\partial \mathscr{F}_e}{\partial r}$ at the boundary:

$$\left[(1 + \epsilon)^2 \gamma'(\epsilon) - \frac{\partial \mathscr{F}_e}{\partial r} \right]_{r^+}^{r^-} = 0 \,. \tag{1.41}$$

This second boundary condition is driven by the Shuttleworth effect at the boundary.

With the boundary conditions the equilibrium geometry problem becomes an energy minimisation problem which can be treated with variational methods:

$$\mathscr{F} = \mathscr{F}_e + \sum_i \int_{-\infty}^{r_i} \gamma_i(\epsilon)\, \mathrm{d}s\,. \tag{1.42}$$

The specific geometry will depend on material properties and the no pinning conditions may not be universally applicable and we therefore reserve application to the extent necessary to study dynamics. Nevertheless, there is an important result that follows from such an analysis in the case of small linear strains. When the no pinning condition applies, it is possible to have a change in the microscopic contact angle, θ_S, from film strain without a corresponding change in θ_L. Although this is associated with larger strains and is driven by the Shuttleworth effect, we must be careful in considering how to connect a macroscopic droplet contact angle measurement to behaviour.

1.4 Dynamics

1.4.1 Rheology Definitions

Rheology is the study of the deformation and flow of materials. We use a graphical representation (Fig. 1.9) to illustrate some of the basic concepts in this field. We first look at a material's shear strain, λ, in response to a step function in stress (Fig. 1.9a). In a perfectly elastic material $\lambda \propto \sigma$, according to eq 1.29 and we get another step function in λ. In contrast, a liquid will have an increasing shear given a constant

stress. The slope of this relationship defines the viscosity, μ of the material[4]:

$$\mu = \frac{\sigma}{\lambda}\,. \tag{1.43}$$

In general, viscosity can be a function of parameters, commonly including the shear rate, $\dot{\lambda}$ (Fig. 1.9b). If the material has both elastic and viscous characteristics, it is referred to as viscoelastic. In the case when viscosity is constant with respect to λ and $\dot{\lambda}$ the liquid is said to be Newtonian and we use the notation $\mu_o = \eta$. Like with Young's modulus for solids, viscosity can be used to define different flow regimes in fluids, simplifying the physics. We consider comparisons of viscous forces with diffusion, surface tension, and inertial forces.

Looking at a small enough scale, we must consider the molecular properties of fluids. Brownian motion will cause random motion of the molecules resulting transport of mass that competes with mechanical flow. To account for these forces we can average the mass diffusion through some area per unit time to get the mass diffusion coefficient, D. We can now compare these effects to the bulk or advective flow through the same area, through what is known as the Peclet number, Pe.

$$\text{Pe} = \frac{lv}{D}\,, \tag{1.44}$$

where l is a characteristic lengthscale and v a characteristic velocity. If Pe $>> 1$, which is generally true in the systems we analyse, we are dominated by bulk flow and can ignore diffusion.

Next we introduce the capillary number, Ca, (not to be confused with the capillary

---

[4]We use the dynamic viscosity definitions, the second commonly used viscosity definition, kinematic viscosity, is simply the ratio of dynamic viscosity to material density ρ.

length) which compares viscous forces to capillary forces:

$$\mathrm{Ca} = \frac{\eta v}{\gamma} \, . \tag{1.45}$$

Here a large Ca >> 1 would mean we can ignore surface tension forces. With much of our analysis we are interested in problems where Ca $\sim$ 1 and there is a competition between viscous and capillary forces. Since the viscosity of the substrate and droplet are generally different, the capillary number is not uniquely defined for a droplet on a soft substrate.

Finally, we define the Reynolds number Re which is the ratio of inertial and viscous forces on a fluid:

$$\mathrm{Re} = \frac{\text{inertial forces}}{\text{viscous forces}} = \frac{\rho v l}{\eta} \, , \tag{1.46}$$

where ρ is the material density, v is fluid velocity l is a characteristic lengthscale for the system. If Re >> 1 the flow is dominated by inertial effects and is more likely to have what is known as turbulent flow where there are chaotic changes in pressure and velocity in the fluid. When $\eta << 1$ the flow is said to be laminar or viscous. In many cases, our systems will have low Reynolds numbers and we will be able to ignore inertial effects.

1.4.2   Bulk viscous dissipation

To understand dissipation in the bulk we can start with momentum conservation. Using this principle we can establish a continuity equation that relates the flow at at any point in a material to the stress tensor and external forces at that point [28–30]. Our approach will involve finding both sides of Newton's second law, $\frac{\mathrm{d}p}{\mathrm{d}t} = F_{net}$, of

an infinitesimal volume. Looking at the left side, we establish the material derivative $\frac{Df}{Dt}$ for time and position dependant properties:

$$\frac{Df}{Dt} = \frac{\mathrm{d}}{\mathrm{d}t} f(\mathbf{x}, t) , \tag{1.47}$$

$$= \frac{\partial f}{\partial t} + \mathbf{v} \cdot \boldsymbol{\nabla} f . \tag{1.48}$$

Using this notation the left side becomes:

$$ma = \int_V \rho \frac{D\mathbf{v}}{Dt} \, \mathrm{d}V , \tag{1.49}$$

where, $\mathbf{v}$, is the velocity field. Next we look to rewrite the net force on our infinitesimal volume. We note that the stress tensor, $\bar{\bar{\sigma}}$ can give us the force acting on each surface of our infinitesimal volume. We can then integrate over the surface to get the total force. We also add any external acceleration, f to give:

$$F_{net} = \int_{\mathbf{S}} \bar{\bar{\sigma}} \cdot \mathrm{d}\mathbf{S} + \int_V \rho \mathbf{f} \, \mathrm{d}V . \tag{1.50}$$

Using the divergence theorem we can rewrite the surface integral as a volume integral, and comparing integrands of $\frac{\mathrm{d}p}{\mathrm{d}t}$ and F_{net} we have the Cauchy momentum equation:

$$\rho \frac{D\mathbf{v}}{Dt} = \boldsymbol{\nabla} \cdot \bar{\bar{\sigma}} + \rho \mathbf{f} . \tag{1.51}$$

This equation applies for any continuous media. To make problems more tractable, a common practice is to split pressure, p, from viscous drag. To complete the separation, we assume that the relationship between $\bar{\bar{\sigma}}$ and velocity gradients is linear and isotropic so we can split $\bar{\bar{\sigma}}$. This allows the perpendicular and shear components of

the stress tensor to be written as follows:

$$\sigma_{ii} = -p + \lambda \boldsymbol{\nabla} \cdot v + 2\mu \frac{\partial \dot{x}_i}{\partial x_i} \, , \tag{1.52}$$

$$\sigma_{ij, i \neq j} = \mu \left(\frac{\partial v_i}{\partial x_j} + \frac{\partial v_j}{\partial x_i} \right) \, , \tag{1.53}$$

where λ is known as the volumetric, or bulk viscosity associated with compression and expansion as opposed to shear. For many fluid flows we can also assume that density is constant through the volume, the so called incompressible flow condition. In this case $\boldsymbol{\nabla} \cdot \mathbf{v} = 0$ and have:

$$\sigma_{ij} = -p\delta_{ij} + \mu \left(\frac{\partial v_i}{\partial x_j} + \frac{\partial v_j}{\partial x_i} \right) \, . \tag{1.54}$$

Substituting this result back into the Cauchy momentum equation we arrive at the incompressible form of the Navier-Stokes equation:

$$\rho \frac{D\mathbf{v}}{Dt} = -\boldsymbol{\nabla} p + \mu \nabla^2 v + \rho \mathbf{f} \, . \tag{1.55}$$

We can now find a simple form for the dissipation is a volume of material by writing out the kinetic energy in a portion of fluid:

$$E_{kin} = \frac{1}{2}\rho \int v^2 \, \mathrm{d}V \, , \tag{1.56}$$

Substituting in eq. 1.55 and noting the incompressibility condition as well as no fluid motion at infinity we find the energy dissipation per unit volume in a material [28]:

$$\dot{E}_{kin} = \frac{1}{2}\eta \left(\dot{\varepsilon}_{ij} \right)^2 \, . \tag{1.57}$$

27

Equation 1.57 applies to a fluid of viscosity, η, however, we will see that it is not necessarily limited to Newtonian fluids.

1.4.3   Viscoelastic materials

To analyse viscoelastic materials using the Navier-Stokes equations we exploit the fact that we study droplets moving at a constant velocity. In this case, a transformation to the frequency domain allows us to more simply account for the shear rate dependence of the viscosity. To develop a simplified frequency domain picture we hold to conditions of the incompressible Navier Stokes equation [31]. As such, the material must be linearly viscoelastic (μ independant of the magnitude of ϵ). This allows us to find the time differential stress $\mathrm{d}\sigma = \mu\,\mathrm{d}\varepsilon = \mu\dot\varepsilon\,\mathrm{d}t$) and the stress-strain relationship becomes [31]:

$$\overline{\overline{\sigma(\mathbf{x},\mathbf{t})}} = \int_{-\infty}^{t} \mu(t-t')\dot{\overline{\overline{\varepsilon}}}(t')\,\mathrm{d}t' - p(\mathbf{x},t)\overline{\overline{\mathbf{I}}}. \tag{1.58}$$

We can convert to the frequency domain with the transformation:

$$\mu(\omega) = i\omega \int_0^{\infty} \mu(t)e^{i\omega t}\,\mathrm{d}t \ . \tag{1.59}$$

In a purely elastic material, we expect the stress to be perfectly in phase with this stress, whereas it should lag by $\pi/2$ for a pure viscous phase. We therefore can define our complex modulus as follows:

$$\mu(\omega) = G'(\omega) + iG''(\omega) \ . \tag{1.60}$$

Where $G'(\omega)$, the storage modulus, accounts for the elastic portion of the modulus and $G''(\omega)$, the loss modulus, accounts for the viscous portion. Now we can write each component of our stress strain matrix as follows [31]:

$$\sigma_{ij}(\mathbf{x}, \omega) = \mu(\omega)\varepsilon_{ij}(\mathbf{x}, \omega) - p(\mathbf{x}, \omega)\delta_{ij} . \tag{1.61}$$

Since cross-linked rubbers have a Poisson ratio close to 0.5 and can be treated as incompressible, this equation is applicable [11]. In these systems, the Chasset-Thirion equation [32, 33] is commonly used to model a complex modulus:

$$\mu(\omega) = \mu_o \left(1 + (i\omega\tau)^{-m}\right) . \tag{1.62}$$

Where μ_o is the material storage modulus, τ is a relaxation time and m is a system dependant exponent. We will treat this as an empirical relationship where each parameter can be extracted from rheological measurements.

1.4.4   Complications in droplet dissipation

Although the bulk viscous dissipation picture is valid for the volume of the droplet and substrate, the picture fails in the region immediately surrounding a mathematically sharp contact line. The failure of this model is due to Huh and Sciven's paradox [34, 35]. We imagine a solid surface moving at velocity, V, under a wedge of fluid with small contact angle, θ. In this region we can then assume that that the height of the droplet, $h(x) \approx \theta x$. We apply a standard no-slip boundary condition where the velocity of the liquid and solid must be equivalent at the point of contact and so
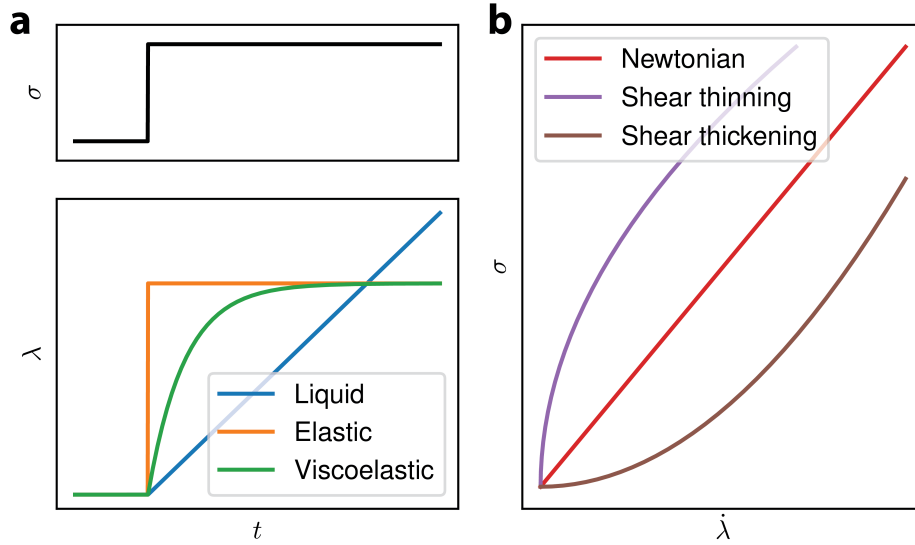
Figure 1.9: a) Plot of the stress and corresponding strain against time for a set of materials. b) Plot of stress against stain for an example set of liquids with varying rheology.

our velocity gradient $\frac{\mathrm{d}v_x}{\mathrm{d}z} = \frac{U}{\theta x}$. According to eq. 1.57 we then have:

$$D_{visc} \approx \eta \int_{x_1}^{x_2} \left(\frac{V}{\theta x} \right)^2 \theta x \, \mathrm{d}x = \frac{\eta V^2}{\theta} \ln x_2/x_1 \, ; \qquad (1.63)$$

where x_1 defines the contact point and x_2 defines some droplet lengthscale. If we let $x_1 = 0$ and integrate over the entire edge, we find the result diverges. Since droplets do in fact move, we must include microscopic corrections to the bulk viscous picture when dealing with the contact line.

Real droplets also introduce contact angle hysteresis and pinning which may affect dissipation measurements [13]. We define contact angle hysteresis through a hypothetical experiment. We consider two paths to reach a given droplet volume on a sample substrate. We could start with a bare substrate and slowly deposit until we

reach the required volume. We call the the droplet contact angle during this application the advancing contact angle, θ_a. Conversely, we could remove liquid from a larger droplet until it reaches the required volume. The angle measured here is the receding contact angle, θ_r. For many substrates we find that $\theta_a > \theta_b$ [35]. The difference $\delta\theta = \theta_a - \theta_r$ describes the degree of contact angle hysteresis in the system.

There are several mechanisms that lead to this hysteresis. The first mechanism involves microscopic imperfections in the surface such as dust or chemical inhomogeneities. As the contact line moves over such as surface the potential energy barriers will cause it to pin and and depin on imperfections, changing the droplet contact angle [35]. Similar effects happen with nanometric imperfections which cannot be measured in terms of individual pinning events, however, have a similar effect in resulting in hysteresis. Careful experiments changing the quantity of these imperfections on a surface has shown that $\delta\theta$ does indeed scale with imperfection quantity, with the effect driven by a decrease in the receding contact angle [36]. Although these effects act in addition to dissipation due to substrate softness which are interested in studying, there are methods for accounting for them. The larger microscopic dust particle associated pinning will only result in spikes in dissipation as a droplet moves across a surface which can be ignored. Careful choice of substrate can minimise the hysteresis associated with nanometric effects, for example PDMS films often have minimal hysteresis [10, 20].

1.4.5 Dissipation due to moving contact ridge

There have been a number of studies on theoretical and experimental details of the dynamical wetting of soft substrates. These include studies on the shape of the capillary ridge upon on droplet motion [12] and a form of pinning in stick slip dissipation along the capillary ridge in certain velocity regimes [37].

We are interested in substrate thickness dependant steady state dissipation. To this end we follow a model from a similar system studied by Zhao et. al. [10]. This model builds heavily on previous work on static films by Dervaux et. al. and dynamic wetting by Long. et. al. [11, 38]. We start with determining the equilibrium shape of a static ridge. Since the size of our droplet is much larger than the size of our ridge, we can use a 2D description of the ridge geometry. We also constrain our analysis to an incompressible linear elastic material such that at equilibrium we have:

$$\nabla \cdot \overline{\overline{\sigma}} = \mathbf{0} \,, \tag{1.64}$$

$$\nabla \cdot \mathbf{u} = 0 \,. \tag{1.65}$$

We consider the case where the soft substrate is of initial height h_o and bounded underneath by a infinitely stiff substrate. This means:

$$\mathbf{u}(x, -h_o) = \mathbf{0} \,. \tag{1.66}$$

The model assumes no jump in traction across the substrate ($\gamma_{sl} \sim \gamma_{sv}$). Using our unit tangent to surface $\mathbf{t}$ and normal to surface $\mathbf{n}$ means the boundary condition eq.

1.39 condition simplifies to:

$$\bar{\bar{\sigma}} \cdot \mathbf{n} = \gamma_s \mathbf{n} (\nabla \cdot \mathbf{n}) . \tag{1.67}$$

With this model, σ and u are linearly related and with Fourier analysis (see [10]) we can find the surface profile $u_y(x, y = 0) = \zeta(x)$ given an arbitrary stress distribution at the surface.

To address dynamics, the model allows the surface traction to vary with time. Using the differential form of the Navier-Stokes equations and further Fourier analysis the substrate dissipation can be determined (see Zhao et. al [10]). The substrate dissipation can be balanced with energy injected by the capillary force to find the power dissipation per unit length in a substrate of height h_o:

$$\mathscr{P}_{diss} \propto \mu_o v (v\tau)^m \left(\frac{\gamma h_o{}^3}{\mu_o} \right)^{(1-m)/4} . \tag{1.68}$$

Where for the cases relevant to this thesis, v, is the speed of the droplet moving across the substrate and m the Chasset-Thirion exponent. Equation 1.68 is applicable in the thin film limit where $h_o < l_e$. As $h_o >> l_e$ we are in the bulk regime and the dissipation becomes independant of h_o.

The most direct method of measuring this dissipation is with a force measurement. Assuming dissipation only occurs in the substrate, we expect the dissipation in the system to be given by:

$$\mathscr{P}_{diss} = F_{drop} v . \tag{1.69}$$

With a force dissipation relationship, we have an experimentally measurable quantity we can use to measure dissipation in our system.

Chapter 2

Experimental details

2.1 Samples

2.1.1 Silicone chemistry

Much of the work done on the wetting of soft substrates uses commercially available PDMS formulations, most often SylGard (Dow Corning). This material is generally coated onto a substrate using either dip coating or spin coating [6, 10]. However, commercial solutions are not the ideal cross-linked chains that are necessary for our smaller scale experiments. These solutions have proprietary chemistries with possible additives to improve mechanical properties which may affect the nanoscale chemistry. Furthermore, when a PDMS rubber is cured (i.e. heated with a catalyst to create cross-linking), some chain remain uncrosslinked [39]. The uncrosslinked chains modify dynamics [39] and with thicker films, these chains are difficult to remove. To this end we employ a custom PDMS rubber made from pure PDMS chains.

In general, PDMS is defined as any polymer based on the silicon, oxygen repeating

unit in the polymer backbone outlined in Fig 2.1a. Along with this base structure, functional groups can replace portions of the chain to modify behaviour. In our particular case, we chose a polymer with two functional groups to allow cross-linking. These functional groups are split between two molecules, one referred to as the cross-linker and the other the main chain. In the cross-linker the end groups are replaced by a double bonded structure. In the main chain, $\sim$5% of monomers are replaced by a group that bonds to the aforementioned end groups. By controlling the relative size of each molecule we can achieve several different chain configurations (Fig 2.1). If we have a short main chain and long cross-linking agent, we get a 'star' like network (Fig 2.1b). Conversely, with short cross-linkers we get a structure more akin to a vulcanized, sulfer cross-linked rubber (Fig 2.1c). In the interest of keeping the viscosity of each sub-component equal, we operate in a regime of equally long cross-linker and main chain (Fig 2.1d).

2.1.2 Sample preparation and characterisation

We acquire uncrosslinked PDMS chains from Gelest. We choose the cross-linker (DMS-V35) and the main chain (HMS-064) (PDMS chemistry was done in partnership with Harry Lu and Mike Brook, Department of Chemistry). These reagents are have high viscosity ($\sim$ 7000 cS) as well as similar viscosity which we find aids in spin coating consistency. We mix the materials in a stoichiometric ratio (20:1 cross-linker:main chain) to minimise uncrosslinked chains. Note that a stoichiometric ratio gives the maximum possible stiffness of the material and by modifying this ratio, materials can be made softer as necessary. To prepare PDMS solutions for spin coating we dilute our mixture with toluene to a desired concentration and mix initially using a glass
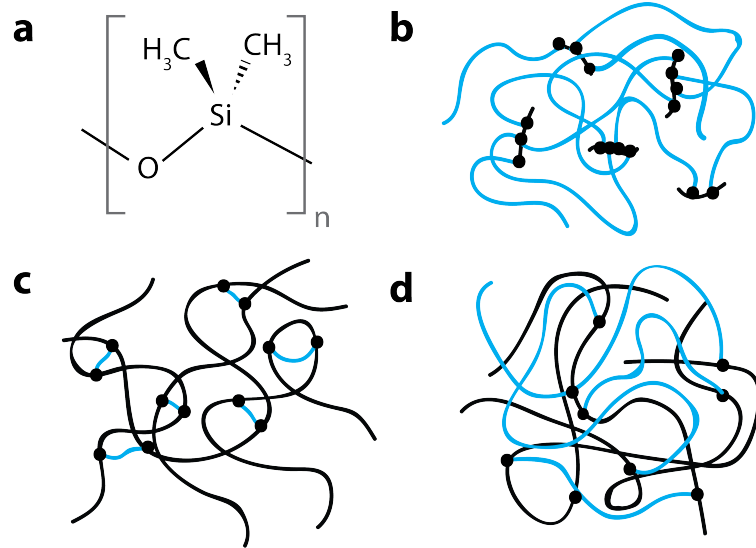
Figure 2.1: a) The main monomer in PDMS polymers, the CH_3 groups are often replaced by a functional group. b) Starlike polymer structure with longer cross-linkers and shorter main chains c) Traditional rubber structure with shorter cross-linkers d) Similar length cross-linking and main chains which we use.

Pasteur pipette, followed a 24hr mix by a lab shaker (Thermo Scientific MAXQ2000).

To characterise bulk mechanical properties we first cure a small $\sim 1\,cm^3$ cube of our mixture at $80\,°C$ for 24hrs. This sample is then placed on a microscope slide on a standard microbalance. We compress this cube using a second slide which is translated vertically using a digital micrometer. With this method we are able to measure a force displacement curve for our cube of material. Any movement in the slide and balance itself (generally minimal) is accounted for using the same measurement without a sample [1]. To calculate the Young's modulus we assume an incompressible material and extract the slope of a pressure-strain plot. We determine the modulus in this

---

[1]We assume the measured effective spring constant follows a simple series spring formulation: $k_{measured} = \left(\frac{1}{k} + \frac{1}{k_o} \right)^{-1}$ where k is the spring constant of the material and k_o is the no-sample spring constant

case is $\sim 100\,\mathrm{kPa}$.

To prepare films we first cleave $\sim 1\,\mathrm{cm}^2$ sections of Si (University Wafer, 100) in a laminar flow hood. These can optionally be cleaned in UV Ozone. We then add diluted PDMS solution to a wafer and immediately spin coat using a Speciality Coating Systems P6000. We keep our spin coater settings constant with maximum acceleration, 3500 rpm spin speed and 1 minute spin time. We use the concentration of PDMS in toluene to control the thickness ranging from $1\,\mathrm{\mu m}$ for 20% wt/wt PDMS and to $25\,\mathrm{nm}$ for 1% wt/wt PDMS. We then cure the films for 2 hrs at $80\,^\circ\mathrm{C}$. To remove uncrosslinked chains, we add toluene to a cured sample, wait $60\,\mathrm{s}$ and spin coat off the excess solution. We repeat toluene addition-spinning process 3 times after which time we add samples to a large volume of toluene and wait 24 hrs before spinning off excess a final time. These films are characterised for thickness by elipsometry (Accurion EP4) and for uniformity by AFM (Bruker Multimode) (Fig 2.2a). To ensure uncrosslinked chains are washed off, elipsometry measurements are taken with different washing times until further washing does not decrease thickness (Fig 2.2b). We confirm the chains are washed off by measuring the contact angle of a droplet before and after a long time period to ensure it is independent of time.

Along with film choice, it is also important to choose an appropriate droplet liquid. We choose the ionic liquid, 1-ethyl-3-methylimidazolium dicyanamide (Sigma-Aldrich) based on three primary criteria. First, at the lengthscales of the droplet studied ($\sim 100\,\mathrm{\mu m}$), the surface area to volume ratio is large and evaporation is a concern. With a vapour pressure approaching zero, the ionic liquid essentially eliminates this problem. Secondly the liquid must have a fairly low viscosity since we are interested in dissipation in the substrate, not the droplet itself. The viscosity of our
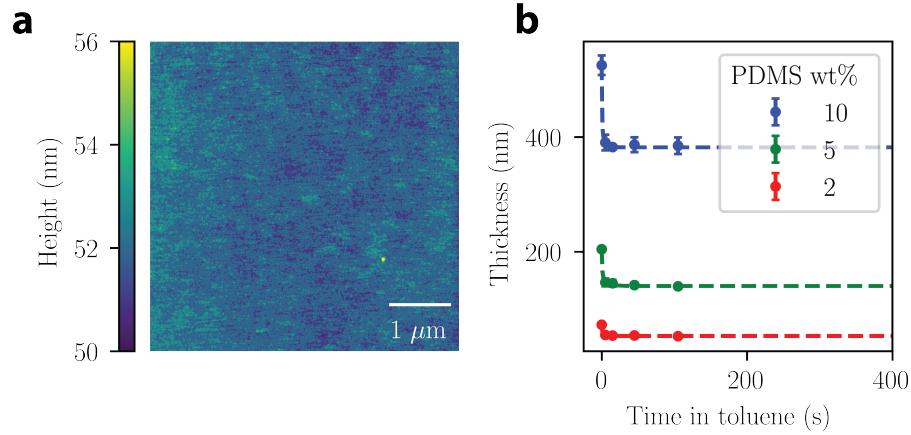
Figure 2.2: a) Sample atomic force microscopy image of a PDMS film thickness (52 nm) taken using (Bruker Multimode) b) Thickness vs time in toluene for an assortment of PDMS film thicknesses at given starting concentrations.

ionic liquid is 21 cP [40], while this is higher than water at $\sim$1 cP, the viscosity of the ionic liquid is much lower than our substrate ($\sim$7000 cP). Finally, the liquid should have a large contact angle with the substrate to allow for a more mobile, easier to study droplet. Although this exact value will depend on the substrate, we find this ionic liquid does have a sufficiently high contact angle on PDMS.

2.2 Apparatus

2.2.1 Measurements

To measure forces we use the micropippette deflection technique outlined in several papers by our group [41–43]. First we pull a glass capillary (diameter 1 mm) using a heating element and constant force puller (Narishige PN-31) to a desired diameter ($\sim$10-100 μm) [2]. We melt the end of the pipette closed to avoid any aspiration of

---

[2]For thicker diameters a more rudimentary flame heating with elastic band pulling is effective

the droplet. This pipette acts as a force sensing rod with a defined spring constant based on thickness and length. From images of the pipette, we use cross-correlation image analysis to measure pipette deflection to sub-pixel ($\sim 1/3$ pixels) precision and are able to measure forces as low as $10\,\mathrm{pN}$ [41]. We then calibrate the pipette spring constant using small known masses (copper wire). This pipette can be inserted into a droplet to measure the total droplet surface interaction force. Note that this causes some deformation of the droplet, however, the substrate dissipation occurs at a much smaller lengthscale far from the pipette and as such is likely unaffected.

Our home-built imaging setup is outlined in Fig 2.3. We first attach the silicon wafer to a motorised translation stage (Newport LTA-HS) which can move at speeds ranging from ($0.1\,\mathrm{\mu m/s}$ to $0.5\,\mathrm{mm/s}$). Since we operate in the regime where surface tension dominates gravity, the substrate can be placed into any orientation depending on application. To manipulate droplets, we include two pipettes, one open to aspirate droplets and the other closed for force sensing. The system must be aligned such that the pipette-surface separation distance remains constant to within several microns over a large ($\sim 5\,\mathrm{mm}$) translation range. The droplet is imaged with a collimated backlight to allow for dark contrasting edges. We image the droplet at a shallow angle ($\sim 2°$ which allows for an image of the droplet and its reflection in the substrate. A secondary simultaneous top down view has also been developed but is not used in analysis (Fig 2.4b). In a typical experiment, we aspirate a small volume of ionic liquid onto the substrate and allow it to equilibriate with the environment for 24 hrs. We then move the substrate back and forth at a constant speed over a typical distance distance of $\sim 0.5\,\mathrm{mm}$, since the pipette holds the droplet in place, we create relative motion of the droplet. The images of the profile of the droplet are taken at regular
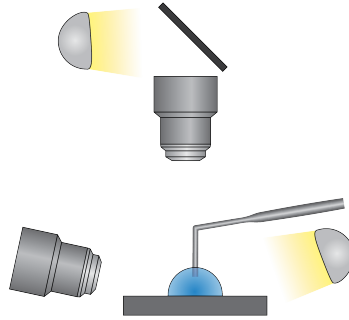
Figure 2.3: Sketch of the apparatus in use for imaging and force sensing droplets in motion. Note that the substrate is moved in and out of the page and the pipette would be out of plane in reality. The aspiration pipette is retracted from the droplet during experiment and not shown here.

intervals throughout the motion.

2.2.2   Analysis

To find contact angles, we use an edge detection algorithm to find the outline of the droplet (Fig 2.4a). This algorithm is able to exclude any dust particles and internal refractions in the droplet with connectivity analysis [44]. The sharp transition between the dark droplet and the air means the droplet profile is known to the micron lengthscale. The edge of the droplet can be found by the slope discontinuity at the droplet reflection or the maximum horizontal extent of the droplet. We then perform an empirical parabolic fit to each edge of the droplet to determine a contact angle. Droplet radius is simply determined by the difference between the edge locations.

For each frame in a video, we perform cross-correlation analysis by taking the the intensity profile along a slice of the image containing the pipette. This intensity profile is then shifted horizontally pixel by pixel to create an array of shifted intensity profiles. These profiles are compared to a reference profile for an an unforced pipette

using a standard cross-correlation definition ($c_{av}[k] = \sum_n a[n+k] * \overline{v[n]}$ where a and v are the functions to compare). By finding the peak of this cross-correlation curve using a Gaussian fit, we can find a sub-pixel value for the displacement of the pipette.

Each of the contact angle and force measurements is repeated for each frame in the experiment where the droplet is held is place as the substrate moves back and forth. This process results in a series of force plateaus with spikes causes by the microscopic defects such as dust particles (Fig 2.4c). We extract the smooth, horizontal regions from these plateaus to get a value for the steady state force, and therefore dissipation, in our system.
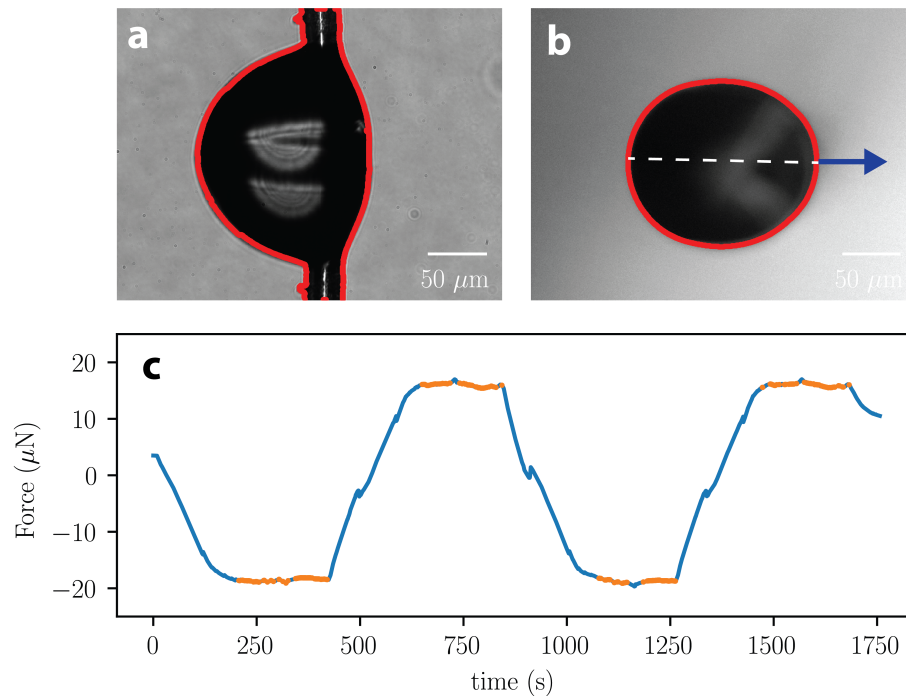
Figure 2.4: a) Side profile as well as edge detection of a sample droplet on a substrate. Note that the droplet is mirrored on the substrate. The cross correlation value is taken using a slice of the pipette near the droplet. b) Sample top down view of a droplet with edge detection. The dotted line indicates the symmetry axis of the droplet and the arrow points in the direction of droplet motion. Although we have developed this technique, results included in this thesis are from versions of the experiment without the top down view. c) Plot of force vs time for a sample run ($v = 2\,\mu\text{m/s}$ and $h_{film} = 150\,\text{nm}$ and example of plateau extraction (in orange) to determine steady state forces. Note that the spikes represent the droplet going over dust particles, and are repeated in the same location for multiple runs.

Chapter 3

Results

To explain our results, we build a simple scaling model that incorporates the features of the more complex model outlined in [10]. We start with the idea that dissipation is dominated by the contact line and should scale with the perimeter of the droplet. If we assume that there is minimal elongation of the droplet, the perimeter should in turn scale with radius of the droplet, r. There are two sources for this dissipation, either from viscous flow in the droplet, P_d, or viscous flow in the substrate, P_s (Fig 3.1a):

$$\mathscr{P}_{diss} \propto r \left(P_s + P_d \right) . \tag{3.1}$$

Both the dissipation terms should scale with viscosity. Since we only consider systems where $\eta_s >>> \eta_d$ the droplet dissipation term is neglected. Next, since the dissipative term in the Chasset-Thirion equation has power law frequency behaviour we posit that dissipation in the substrate will similarly scale with v^n where n is an
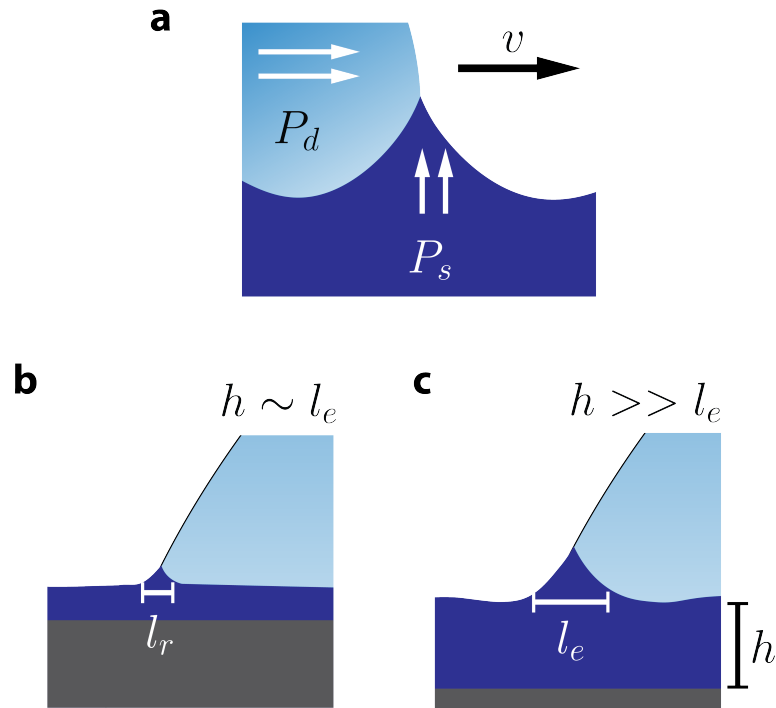
Figure 3.1: a) Schematic close up of capillary ridge indicating dissipation occurring at the edge of the droplet and in the substrate. b) Case where the substrate thickness, h, is comparable to the elastocapillary length, l_e such that $l_r < l_e$. c) Case where $h >> l_e$ such that $l_r \sim l_e$

exponent not necessarily equal to the exponent m from the Chasset-Thirion equation.

$$\mathscr{P}_{diss} \propto r\beta(h)v^n \,, \tag{3.2}$$

where $\beta(h)$ is a parameter introduced to account for substrate thickness effects. To find the form of this parameter we assume that the dissipation in a ridge will scale with its volume. A larger ridge should result in greater dissipation. We call the lengthscale of the ridge, l_r (Fig 3.1b), and per unit length we then have:

$$\beta(h) \propto l_r{}^2 \,. \tag{3.3}$$

There are two distinct scaling regimes. In the case where the film height is much greater than the elastocapillary length ($h_o >> l_e$) we are in the bulk regime where $l_r = l_e$ (Fig 3.1c). Below l_e we expect l_r to decrease as film height decreases (Fig 3.1b). It can be shown in the thin film regime the ridge size scales with $h^{3/2}$ [10]. Combining all of this we have:

$$\beta(h) \propto l_r{}^2 \sim \begin{cases} l_e{}^2 & \text{if } h_o > l_e \\[2mm] l_e{}^2 \left(\dfrac{h}{l_e}\right)^{3/2} & \text{if } h_o < l_e \end{cases}$$

To test the validity of our model, we examine each term individually. To test the radius dependence we simply change the size of the droplets keeping all other parameters constant. Although there is deformation of the droplet along the direction they are dragged (Fig. 2.4b), we still find a linear relationship between power dissipated
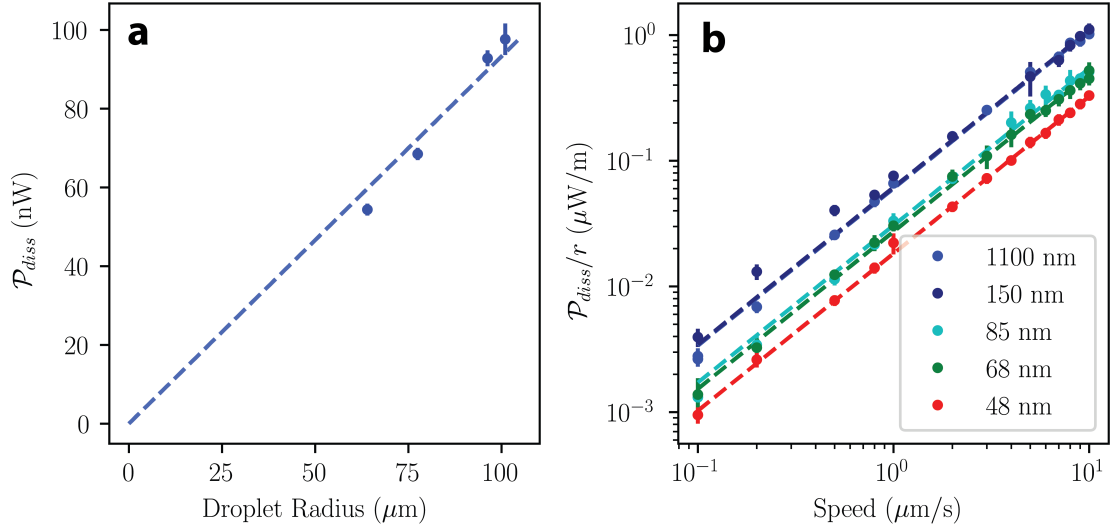
Figure 3.2: a) Plot of dissipation vs droplet radius for a sample substrate (thickness 150 µm at a constant speed ($\overline{9\,\text{µm/s}}$). b) Log-log plots of radius normalised dissipation against speed across a range of thicknesses.

and radius. This indicates that the contact line is indeed the region where the majority of the dissipation occurs. To test the velocity power law, we now normalise dissipation by radius and vary the speed across two orders of magnitude. Plotting on a log-log plot we do indeed see power law behaviour across a range of thicknesses (Fig 3.2b) with $n \sim 7/4$. The intercept of these log-log plots corresponds to the β parameter, and by running several samples we can test the thickness dependence of dissipation (Fig 3.3). Again, we see behaviour consistent with our model, with a $\mathscr{P} \propto h_o$ when $h_o < l_e$ followed by a plateau at bulk film thicknesses. Fitting the data we we find the extracted modulus matches that measured with cube compression tests well (100 kPa). Overall, we see a qualitative match between our model and experiments.
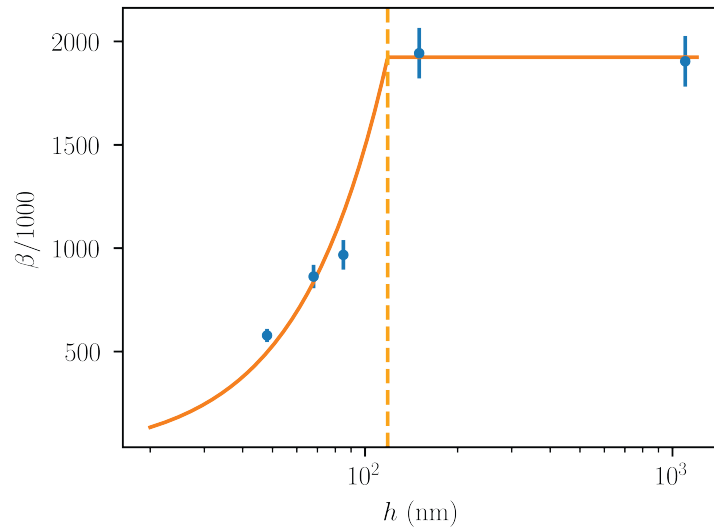
Figure 3.3: Plot of the β parameter against the thickness of the film in a semi-log plot. The curve fit's free parameters include the elastocapillary length.

Conclusions

In this work we explored the physics of soft wetting and in particular how soft dynamics is affected by thickness in the microscopic regime. We prepared samples and built an apparatus that is able measure the force on microscopic droplets in motion. We find that below the elastocapillary length the dissipation increases with the thickness of the film. Above this lengthscale, the dissipation becomes independent of film thickness. These results are in agreement with previous work on larger droplets [10].

The physics of wetting is a complex and growing field and looking forward, there are numerous avenues for future research. Specifically, the ability of our techniques to simultaneously image and measure forces on a droplets in multiple planes opens up several opportunities. For example, droplet force measurements on liquid substrates is difficult since standard gravitational forcing is impossible. Our techniques have no issues with such systems. Furthermore, by operating below the elastocapillary length we could more easily study additional geometries such as free standing films and fibers. Gaining a fundamental physical understanding of such systems could have applications in numerous fields ranging from water collection to microfluidics.

Bibliography

[1] Antonin Marchand, Joost H. Weijs, Jacco H. Snoeijer, and Bruno Andreotti. Why is surface tension a force parallel to the interface? *American Journal of Physics*, 79(10):999–1008, 2011.

[2] Robert W. Style and Eric R. Dufresne. Static wetting on deformable substrates, from liquids to soft solids. *Soft Matter*, 8(27):7177–7184, 7 2012.

[3] Rafael D. Schulman, Amir Porat, Kathleen Charlesworth, Adam Fortais, Thomas Salez, Elie Raphaël, and Kari Dalnoki-Veress. Elastocapillary bending of microfibers around liquid droplets. *Soft Matter*, 13(4):720–724, 1 2017.

[4] Su Ji Park, Byung Mook Weon, Ji San Lee, Junho Lee, Jinkyung Kim, and Jung Ho Je. Visualization of asymmetric wetting ridges on soft solids with X-ray microscopy. *Nature Communications*, 5, 7 2014.

[5] Shih-Yuan Chen, Aaron Bardall, Michael Shearer, and Karen E. Daniels. Distinguishing deformation mechanisms in elastocapillary experiments. *Soft Matter*, 15(46):9426–9436, 2019.

[6] R. W. Style, Y. Che, S. J. Park, B. M. Weon, J. H. Je, C. Hyland, G. K. German, M. P. Power, L. A. Wilen, J. S. Wettlaufer, and E. R. Dufresne. Patterning droplets with durotaxis. *Proceedings of the National Academy of Sciences*, 110(31):12541–12544, 7 2013.

[7] Rafael D. Schulman, René Ledesma-Alonso, Thomas Salez, Elie Raphaël, and Kari Dalnoki-Veress. Liquid Droplets Act as "compass Needles" for the Stresses in a Deformable Membrane. *Physical Review Letters*, 118(19):1–6, 5 2017.

[8] Wang Xi, Fang Kong, Joo Chuan Yeo, Longteng Yu, Surabhi Sonam, Ming Dao, Xiaobo Gong, and Chwee Teck Lim. Soft tubular microfluidics for 2D and 3D applications. *Proceedings of the National Academy of Sciences of the United States of America*, 114(40):10590–10595, 10 2017.

[9] Yongmei Zheng, Hao Bai, Zhongbing Huang, Xuelin Tian, Fu Qiang Nie, Yong Zhao, Jin Zhai, and Lei Jiang. Directional water collection on wetted spider silk. *Nature*, 463(7281):640–643, 2 2010.

[10] Menghua Zhao, Julien Dervaux, Tetsuharu Narita, François Lequeux, Laurent Limat, and Matthieu Roché. Geometrical control of dissipation during the spreading of liquids on soft solids. *Proceedings of the National Academy of Sciences of the United States of America*, 115(8):1748–1753, 2 2018.

[11] Didier Long, Armand Ajdari, and Ludwik Leibler. Static and dynamic wetting properties of thin rubber films. *Langmuir*, 12(21):5221–5230, 10 1996.

[12] S. Karpitschka, S. Das, M. van Gorcum, H. Perrin, B. Andreotti, and J. H.

Snoeijer. Droplets move over viscoelastic substrates by surfing a ridge. *Nature Communications*, 6(1):7891, 12 2015.

[13] Quere Unknown de Gennes, Brochard-Wyart. Capillarity and wetting phenomena: drops, bubbles, pearls, waves. *Choice Reviews Online*, 41(09):41–5349, 2013.

[14] M V Berry. The molecular mechanism of surface tension. *Physics Education*, 6(2):79, 1971.

[15] J O Indekeu. Line tension near the wetting transition: results from an interface displacement model. Technical report, 1992.

[16] M. J.P. Nijmeijer, C. Bruin, A. F. Bakker, and J. M.J. Van Leeuwen. Wetting and drying of an inert wall by a fluid in a molecular-dynamics simulation. *Physical Review A*, 42(10):6052–6059, 1990.

[17] Joost H. Weijs, Antonin Marchand, Bruno Andreotti, Detlef Lohse, and Jacco H. Snoeijer. Origin of line tension for a Lennard-Jones nanodroplet. *Physics of Fluids*, 23(2):022001, 2 2011.

[18] L. Guo and G. H. Tang. Experimental study on directional motion of a single droplet on cactus spines. *International Journal of Heat and Mass Transfer*, 84:198–202, 2015.

[19] Jacco H. Snoeijer and Bruno Andreotti. A microscopic view on contact angle selection. *Physics of Fluids*, 20(5):057101, 5 2008.

[20] Jacco H. Snoeijer, Etienne Rolley, and Bruno Andreotti. Paradox of Contact

Angle Selection on Stretched Soft Solids. *Physical Review Letters*, 121(6):068003, 8 2018.

[21] Piaras Kelly. *Mechanics Lecture Notes: An introduction to Solid Mechanics*, volume 1. University of Auckland, Auckland, New Zealand, 1 edition, 2015.

[22] Richard AL Jones. *Soft condensed matter*, volume 6. Oxford University Press, 1 edition, 2002.

[23] Pierre-Giles de Gennes. *Scaling concepts in polymer physics*. Cornell University Press, 1 edition, 1979.

[24] J. A. Forrest, K. Dalnoki-Veress, and J. R. Dutcher. Interface and chain confinement effects on the glass transition temperature of thin polymer films. *Physical Review E - Statistical Physics, Plasmas, Fluids, and Related Interdisciplinary Topics*, 56(5):5705–5716, 11 1997.

[25] Christopher M. Stafford, Bryan D. Vogt, Christopher Harrison, Duangrut Julthongpiput, and Rui Huang. Elastic moduli of ultrathin amorphous polymer films. *Macromolecules*, 39(15):5095–5099, 7 2006.

[26] R. Shuttleworth. The surface tension of solids. *Proceedings of the Physical Society. Section A*, 63(5):444–457, 5 1950.

[27] L. A. Lubbers, J. H. Weijs, L. Botto, S. Das, B. Andreotti, and J. H. Snoeijer. Drops on soft solids: free energy and double transition of contact angles. *Journal of Fluid Mechanics*, 747:R1, 5 2014.

[28] Lev Davidovich Landau and Evgeny Mikhailovich Lifshitz. *Fluid Mechanics*, volume 6. Pergamon Press, Oxford, UK, 2 edition, 1987.

[29] D. J. Acheson. *Elementary Fluid Dynamics*. Oxford University Press, Incorporated, 1990.

[30] Suzanne Fielding. The basic equations of fluid dynamics. Technical report, Durham University, Durham, United Kingdom, 2005.

[31] John D Ferry. *Viscoelastic Properties of Polymers*. Wiley & Sons, 3 edition, 1980.

[32] Gregory B. McKenna and Richard J. Gaylord. Relaxation of crosslinked networks: theoretical models and apparent power law behaviour. *Polymer*, 29(11):2027–2032, 11 1988.

[33] Thirion P and Chasset R. Viscoelastic relaxation of rubber vulcanizates in extension. *Chimie & Industrie, Genie Chimique*, 97(5):617–626, 1967.

[34] Chun Huh and L. E. Scriven. Hydrodynamic model of steady movement of a solid/liquid/fluid contact line. *Journal of Colloid And Interface Science*, 35(1):85–101, 1 1971.

[35] Daniel Bonn, Jens Eggers, Joseph Indekeu, and Jacques Meunier. Wetting and spreading. *Reviews of Modern Physics*, 81(2):739–805, 5 2009.

[36] Veronique de Jonghe and Dominique Chatain. Experimental study of wetting hysteresis on surfaces with controlled geometrical and/or chemical defects. *Acta Metallurgica Et Materialia*, 43(4):1505–1515, 4 1995.

[37] M. Van Gorcum, B. Andreotti, J. H. Snoeijer, and S. Karpitschka. Dynamic Solid Surface Tension Causes Droplet Pinning and Depinning. *Physical Review Letters*, 121(20):208003, 11 2018.

[38] Julien Dervaux and Laurent Limat. Contact lines on soft solids with uniform surface tension: analytical solutions and double transition for increasing deformability. *Proceedings of the Royal Society A: Mathematical, Physical and Engineering Sciences*, 471(2176):20140813, 4 2015.

[39] Aurélie Hourlier-Fargette, Arnaud Antkowiak, Antoine Chateauminois, and Sébastien Neukirch. Role of uncrosslinked chains in droplets dynamics on silicone elastomers. *Soft Matter*, 13(19):3484–3491, 5 2017.

[40] Douglas R. MacFarlane, Jake Golding, Stewart Forsyth, Maria Forsyth, and Glen B. Deacon. Low viscosity ionic liquids based on organic salts of the dicyanamide anion. *Chemical Communications*, 16(16):1430–1431, 8 2001.

[41] M. J. Colbert, A. N. Raegen, C. Fradin, and K. Dalnoki-Veress. Adhesion and membrane tension of single vesicles and living cells using a micropipette-based technique. *The European Physical Journal E*, 30(2):117, 10 2009.

[42] Matilda Backholm, William S. Ryu, and Kari Dalnoki-Veress. Viscoelastic properties of the nematode Caenorhabditis elegans, a self-similar, shear-thinning worm. *Proceedings of the National Academy of Sciences of the United States of America*, 110(12):4528–4533, 3 2013.

[43] R. D. Schulman, M. Backholm, W. S. Ryu, and K. Dalnoki-Veress. Undulatory microswimming near solid boundaries. *Physics of Fluids*, 26(10):101902, 10 2014.

[44] Pauli Virtanen, Ralf Gommers, Travis E. Oliphant, Matt Haberland, Tyler Reddy, David Cournapeau, Evgeni Burovski, Pearu Peterson, Warren Weckesser,

Jonathan Bright, Stéfan J. van der Walt, Matthew Brett, Joshua Wilson, K. Jarrod Millman, Nikolay Mayorov, Andrew R.J. Nelson, Eric Jones, Robert Kern, Eric Larson, C. J. Carey, İlhan Polat, Yu Feng, Eric W. Moore, Jake VanderPlas, Denis Laxalde, Josef Perktold, Robert Cimrman, Ian Henriksen, E. A. Quintero, Charles R. Harris, Anne M. Archibald, Antônio H. Ribeiro, Fabian Pedregosa, Paul van Mulbregt, Aditya Vijaykumar, Alessandro Pietro Bardelli, Alex Rothberg, Andreas Hilboll, Andreas Kloeckner, Anthony Scopatz, Antony Lee, Ariel Rokem, C. Nathan Woods, Chad Fulton, Charles Masson, Christian Häggström, Clark Fitzgerald, David A. Nicholson, David R. Hagen, Dmitrii V. Pasechnik, Emanuele Olivetti, Eric Martin, Eric Wieser, Fabrice Silva, Felix Lenders, Florian Wilhelm, G. Young, Gavin A. Price, Gert Ludwig Ingold, Gregory E. Allen, Gregory R. Lee, Hervé Audren, Irvin Probst, Jörg P. Dietrich, Jacob Silterra, James T. Webber, Janko Slavič, Joel Nothman, Johannes Buchner, Johannes Kulick, Johannes L. Schönberger, José Vinícius de Miranda Cardoso, Joscha Reimer, Joseph Harrington, Juan Luis Cano Rodríguez, Juan Nunez-Iglesias, Justin Kuczynski, Kevin Tritz, Martin Thoma, Matthew Newville, Matthias Kümmerer, Maximilian Bolingbroke, Michael Tartre, Mikhail Pak, Nathaniel J. Smith, Nikolai Nowaczyk, Nikolay Shebanov, Oleksandr Pavlyk, Per A. Brodtkorb, Perry Lee, Robert T. McGibbon, Roman Feldbauer, Sam Lewis, Sam Tygier, Scott Sievert, Sebastiano Vigna, Stefan Peterson, Surhud More, Tadeusz Pudlik, Takuya Oshima, Thomas J. Pingel, Thomas P. Robitaille, Thomas Spura, Thouis R. Jones, Tim Cera, Tim Leslie, Tiziano Zito, Tom Krauss, Utkarsh Upadhyay, Yaroslav O. Halchenko, and Yoshiki Vázquez-Baeza. SciPy 1.0: fundamental algorithms for scientific computing in Python. *Nature*

Methods, 17(3):261–272, 3 2020.